



Thermal corrosion fatigue crack growth behavior and life prediction of 304SS pipeline structures in high temperature pressurized water

Z.H. Li^a, Y.M. Han^a, Y.G. Zhao^a, S.L. Yang^b, Z.M. Zhong^b, Y.H. Lu^{a,*}

^a National Center for Materials Service Safety, University of Science and Technology Beijing, Beijing 100083, China

^b State Nuclear Power Plant Service Company, Shanghai 200233, China



ARTICLE INFO

Keywords:

Thermal corrosion fatigue
Crack growth rate
Life prediction
Numerical simulation
Stainless steel pipeline structures

ABSTRACT

The influence of transient water temperature changes on the fatigue crack growth behavior of 304SS pipeline structures was studied based on high-throughput testing method through the modification of dual loop circulating water equipment. Results demonstrated that the fatigue crack growth rate gradually decreased with the decrease of cooling rate, and the crack growth rate was exponentially related to the cooling rate. Both the base material and weld of the stepped pipe showed a transgranular cracking mode, and propagated continuously by slip-oxidation mechanism. Compared with the fine equiaxed grain of the base material, the grain in the weld was coarse and the residual strain was large, and the crack growth rate of the weld was obviously higher. Then, the thermal fatigue crack growth rate model for stepped pipes was established by combining finite element thermo-mechanical coupling simulation and three-dimensional crack propagation analysis software, and the model was modified based on the experimental results.

1. Introduction

Thermal fatigue cracks have been found in primary loop recirculation pipes and various other components in nuclear power plants [1–6]. The fatigue crack growth rate of pipeline structures is an important parameter for safety evaluation after defects are discovered during in-service structural inspections [7–9]. The most typical causes of thermal fatigue formation in nuclear power plant pipeline structures are thermal stratification and thermal shock. During the flow of the medium in the pipeline, the hotter and lighter medium will stay above the cooler and heavier medium, resulting in a certain temperature gradient, which is called thermal stratification. It usually occurs in the horizontal straight pipe position that cannot be isolated from the main pipe, such as the thermal safety injection line and the horizontal section of the wave pipe [10,11]. Due to the action of the cold and hot fluid of the main pipe and the branch pipe, these positions will form a more stable thermal stratification. Thermal shock is usually caused by drastic changes in fluid temperature, and its location is usually in the nozzle area (such as the filling nozzle, spray nozzle, etc.) [12,13]. Due to the fact that thermal fatigue is a thermal strain generated by alternating cold and hot water environments, and high temperature water can also corrode pipelines, this type of fatigue caused by alternating cold and hot water can be called thermal corrosion fatigue.

At present, low cycle fatigue and fatigue crack propagation experiments are generally conducted in high temperature water environments to study the thermal corrosion fatigue service conditions that occur in pipeline structures of nuclear power plants, and the

* Corresponding author.

E-mail address: lu_yonghao@mater.ustb.edu.cn (Y.H. Lu).

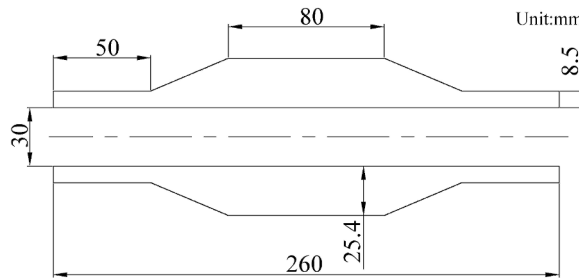


Fig. 1. Specific dimensions of stepped pipe specimens.

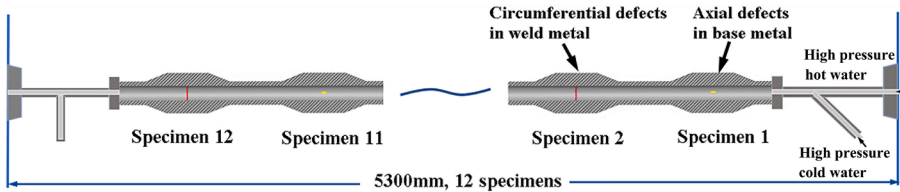


Fig. 2. Schematic diagram of connection and distribution of stepped pipe specimens.

specimens are generally standard round bar specimens and compact tensile (CT) specimens. Many scholars have studied the effects of various factors, such as strain rate [14,15], strain amplitude [16], temperature [17], grain size [18], surface roughness [19], etc. on the low cycle fatigue and crack propagation behavior of 316LN stainless steel in high temperature water environments, revealing the influence of different factors on the corrosion fatigue damage and crack propagation mechanism, and establishing the corrosion fatigue life evaluation model. In addition, some scholars use actual or processed tubular specimens to study the effects of shape factor [20,21], temperature [22,23], dissolved oxygen [24], dissolved hydrogen [25], inclusions [26], etc. on the corrosion fatigue damage mechanism in high temperature water. It is believed that the shape factor has obvious influence on the fatigue life, and a model was used to evaluate the difference in fatigue life between tubular and round bar specimens in high temperature water. Although the academic community has conducted extensive research on high temperature water corrosion fatigue, and there are constantly new research methods and insights into the physical mechanisms of various influencing factors. However, the actual thermal corrosion fatigue is the process of thermal stress generation and fluctuation of pipeline structure due to transient water temperature changes. At present, the design has not fully considered the fatigue failure of components caused by temperature transients [3]. The method of controlling temperature waveform is also lacking to simulate the transient temperature rise and fall of the actual nuclear power pipeline structures to study the thermal corrosion fatigue behavior.

In this study, a device which can simulate the influence of transient temperature change on fatigue behavior of pipeline structure is constructed through the renovation of dual loop circulating water equipment. For typical pressure vessel structures in nuclear power plants, representative stepped pipe structures are selected to conduct thermal corrosion fatigue crack propagation experiments under transient temperature conditions in a simulated primary circuit environment, and the fatigue crack growth rates of stepped pipe structures are obtained. In addition, the thermal fatigue crack propagation life is calculated by finite element method (FEM) and crack propagation analysis software, and the calculation model is modified according to the experiment results.

2. Experimental procedure

2.1. Materials and manufacture of specimen

The experimental materials for this study are the 304 stainless steel base material and 304 stainless steel welded joints provided by the project commissioning party. The specimen is a stepped tubular structure, and its specific dimensions are shown in Fig. 1. In order to study the fatigue crack propagation behavior of stepped pipe specimens, electrical discharge machining was used to prefabricate defects in the inner wall of the stepped pipes. The prefabricated defect form of 304 stainless steel base material is axial defect, and the defect length is 6 mm and the depth is 4 mm. The prefabricated defect at the weld position of 304 stainless steel weld joints is in the form of circumferential defect, with a defect depth of 4 mm. In order to save energy consumption, high-throughput methods are used to conduct thermal fatigue tests. Fig. 2 shows the schematic diagram of connection and distribution of stepped pipe specimens. The specimen close to the inlet of high-pressure cold water and high-pressure hot water is specimen 1. The adjacent two specimens have different types of defects, with singular numbers 1, 3, 5, 7, 9, and 11 indicating axial defects in the 304 stainless steel base material, and numbers 2, 4, 6, 8, 10, and 12 indicating circumferential defects in the 304 stainless steel welded joints. The specimens of different stepped pipes are connected by welding, and the length of the entire bench test section is 5300 mm.

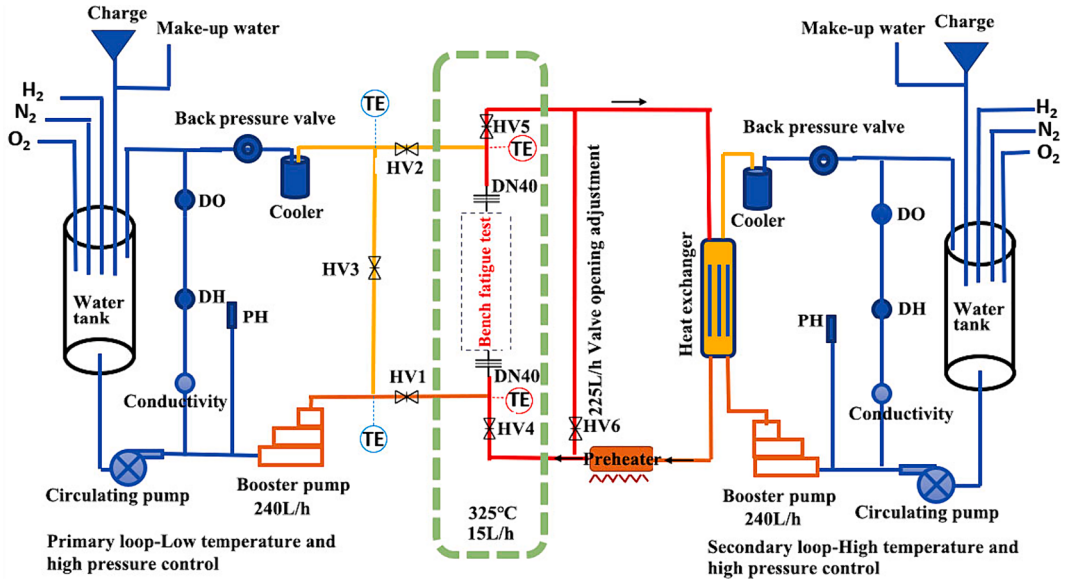


Fig. 3. Schematic diagram of primary loop and secondary loop system of the subcritical water vapor environment structural material test device.

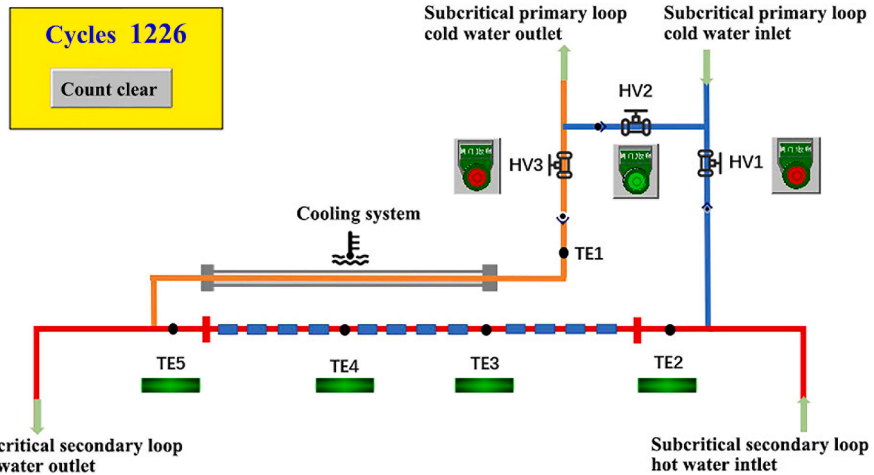


Fig. 4. Schematic diagram for switching between the inlet and outlet of subcritical primary loop cold water and the inlet and outlet of subcritical secondary loop hot water.

2.2. Experimental design and testing method

In order to simulate the thermal corrosion fatigue crack propagation behavior of stepped tubular structures under transient water environment conditions from 325 °C to 38 °C, the combined experiment of the primary loop system and the secondary loop system of the subcritical water vapor environment structural material test device was adopted (Fig. 3). The design maximum operating temperature of the primary loop and secondary loop is 350 °C, the maximum operating pressure is 20 MPa, and the flow rate of the booster pump is 400L/h. The primary loop system serves as a cold water shock component with a flow rate of 240L/h. The secondary loop system, as a high pressure hot water supply component, can control the temperature after cold water shock by adjusting the bypass flow rate, thereby enabling periodic changes in the internal transient temperature of the studied pipeline material between 325 °C and 38 °C. In this experiment, the temperature of the hot water section is 325 °C, the pressure is 15 MPa, and the heating rate is less than 100 °C/h. The temperature of the cold water section is 20 °C and the pressure is 15 MPa. Therefore, the flow rate of the hot water section can be calculated through energy conservation formula (1). Through calculation, when the flow rate of the hot water section of this test is 15L/h, after opening the valve of the cold-water section, the inside of the test pipe can be reduced to about 38 °C.

$$Q_{\text{exo}} = Q_{\text{end}} \quad (1)$$



Fig. 5. Distribution diagram of stepped pipe specimens for actual on-site testing.

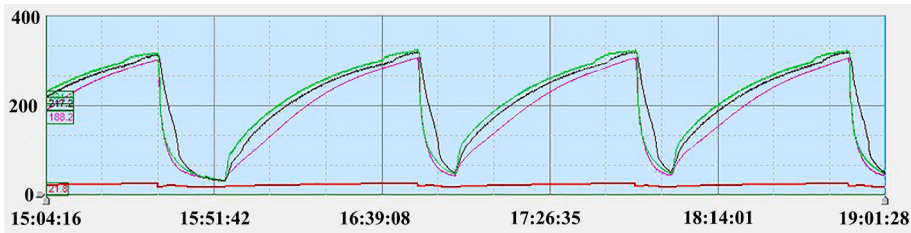


Fig. 6. Variation curve of the actual measured temperature of the inner wall with time during thermal fatigue process.

$$CM_h(t_h - t) = CM_c(t - t_c) \quad (2)$$

where, Q_{exo} is exothermic, Q_{end} is endothermic, M_h is the mass of unit hot water, M_c is the mass of unit cold water, t_h is the temperature of the hot water section at 325 °C, t is the minimum transient control temperature at 38 °C, and t_c is the temperature of the cold water section at 20 °C.

Fig. 4 shows the schematic diagram for switching between the inlet and outlet of subcritical primary loop cold water and the inlet and outlet of subcritical secondary loop hot water. Every four specimens form a group, with a length of approximately 1040 mm. Thermocouples are set at both ends of each group of specimens to monitor the water temperature. Fig. 5 shows the distribution diagram of stepped pipe specimens for actual on-site testing. In this test, the electric heating fiber is directly wrapped on the specimen, which is conducive to rapid heating of the pipeline. In order to test safety, the specimen protection sleeve is set on the outermost part of the specimen to prevent water vapor splashing and other problems. The test device also includes dissolved oxygen, dissolved hydrogen, conductivity and PH probes, which can accurately control the dissolved oxygen content (0–20 mg/L) and dissolved hydrogen content (0–20 mg/L) in the loop, and measure PH and conductivity online. Fig. 6 shows the variation curve of the actual measured temperature of the inner wall with time during thermal fatigue process. By recording the temperature changes per unit time using thermocouples, the average cooling rate of each specimen during cold water impact can be obtained. After 1226 cycles of alternating cold and hot water fatigue testing, crack propagation analysis was conducted on the stepped pipe specimen. Due to the inaccurate temperature control of specimen 1 in actual experiments, this paper will not analyze this specimen.

2.3. Material characterization

Field emission scanning electron microscope (FE-SEM) was used to observe the thermal corrosion fatigue crack propagation morphology with a scanning voltage of 15 kV. In addition, electron back scatter diffraction (EBSD) was used to observe the crack propagation area, and the accompanying CHANNEL 5 software was used to analyze the inverse pole figure (IPF) map and kernel average misorientation (KAM) map. EBSD samples were prepared using vibration polishing method. The vibration polishing solution was 50 nm neutral alumina suspension, with a vibration polishing frequency of 90 Hz and a time of 4 h.

3. Numerical simulation method

In this study, the finite element analysis (FEA) software ABAQUS and the new generation crack analysis software FRANC3D were

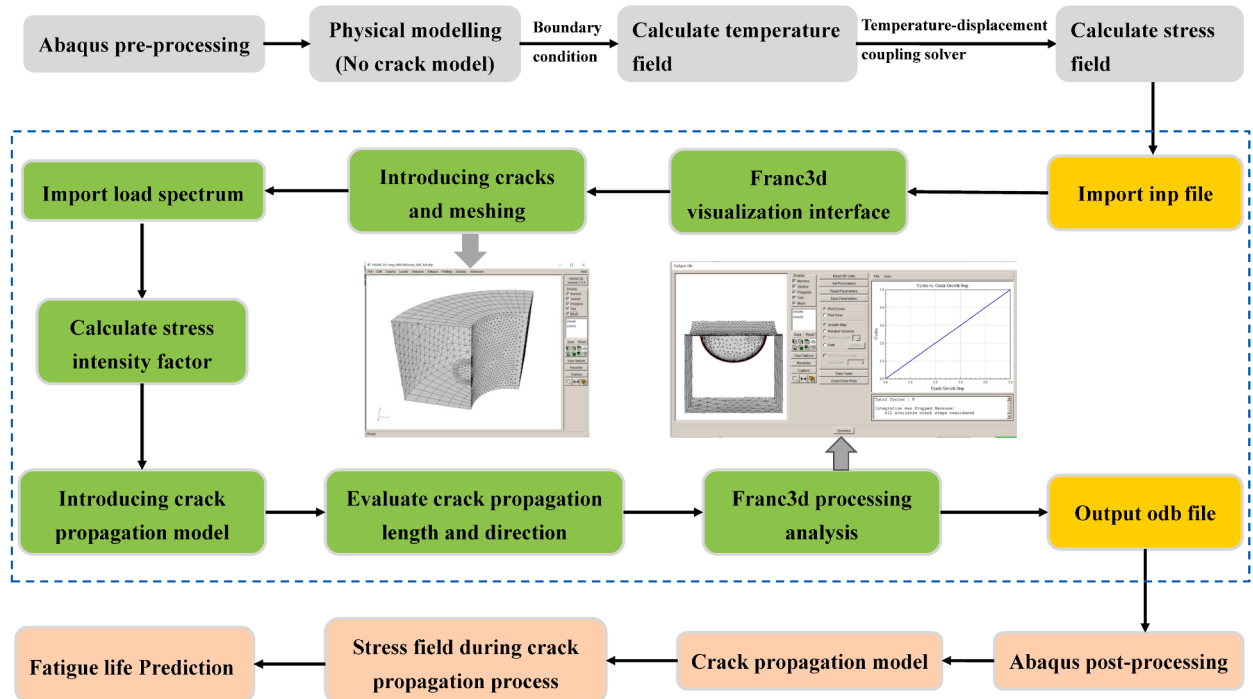


Fig. 7. Numerical simulation flowchart of fatigue crack propagation in 304 stainless steel stepped tubular structure.

Table 1
Mechanical properties of 304 stainless steel at different temperatures.

T (K)	E (MPa)	$\sigma_{0.2}$ (MPa)	σ_b (MPa)	$E_t/\%$	$\Psi/\%$
293	1.81E + 05	540	734	37	72
523	1.85E + 05	438	564	17	64
623	1.84 E + 05	391	527	19	61
673	1.78 E + 05	409	494	18	66
773	1.67 E + 05	373	443	13	66
873	1.60 E + 05	280	339	27	67
973	1.35 E + 05	197	234	59	76

Table 2
Thermophysical parameters of 304 stainless steels at different temperatures.

T(K) Thermophysical parameters	293–373	373–473	473–573	573–673
Linear expansion coefficient ($10^{-6} \cdot ^\circ\text{C}^{-1}$)	16.5	17.2	17.7	18.1
Convective heat transfer coefficient (W/(m ² ·°C))	0.025			
Radiation coefficient	0.8			

used to simulate the thermal fatigue crack propagation of 304 stainless steel stepped tubular structures. Fig. 7 shows the numerical simulation flowchart of fatigue crack propagation in stepped tubular structures. Firstly, the physical modeling of the stepped tubular structure was carried out by ABAQUS software, and the changes in temperature field were calculated by inputting material constitutive parameters, thermophysical parameters, and setting corresponding boundary conditions. Then, the temperature field was taken as the initial condition, and a temperature-displacement coupling solver was selected to calculate the thermal deformation of the stepped pipe without prefabricated cracks. Finally, the stress field of the stepped tubular structure was obtained. Table 1 and Table 2 show the mechanical properties and thermophysical parameters of 304 stainless steels at different temperatures, respectively. Fig. 8(a–b) show the relation between density, specific heat capacity, thermal diffusivity, and thermal conductivity of 304 stainless steel with temperature change, respectively [27]. The boundary condition of the inner wall was the temperature change data of the inner wall of the stepped pipe specimens measured through experiments, as shown in Fig. 8(c). The heat conduction inside the stepped pipe was steady-state nonlinear heat conduction, and its governing equation was as follows:

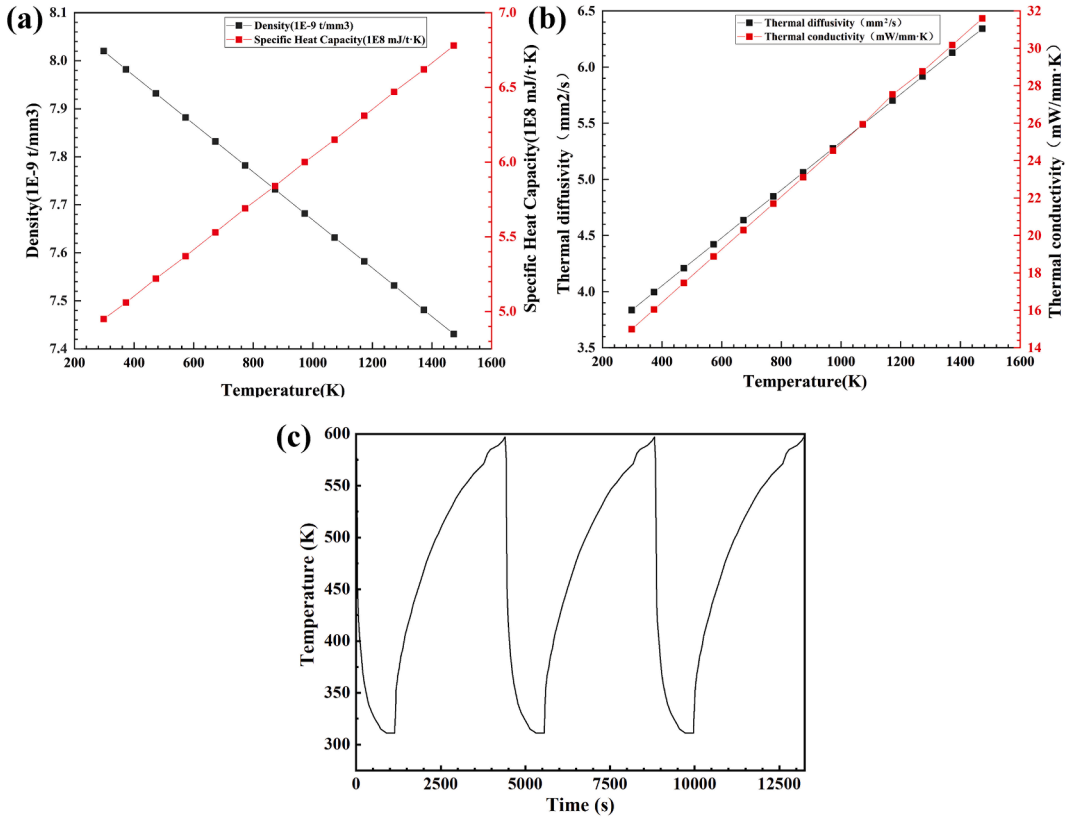


Fig. 8. Thermophysical parameters and test curves: (a) Relation between density and specific heat capacity of 304 stainless steel with temperature change, (b) relation between thermal diffusivity and thermal conductivity of 304 stainless steel with temperature change, (c) actual measured temperature of the inner wall with time during thermal fatigue process.

$$\rho c \frac{\partial T}{\partial t} = \frac{\partial}{\partial x} (\lambda \frac{\partial T}{\partial x}) + \frac{\partial}{\partial y} (\lambda \frac{\partial T}{\partial y}) + \frac{\partial}{\partial z} (\lambda \frac{\partial T}{\partial z}) \quad (3)$$

where ρ , c and λ are the density, specific heat capacity and thermal conductivity of the material respectively, which are all functions of temperature.

The boundary conditions of the outer wall were convective heat transfer Q_1 and radiative heat transfer Q_2 :

$$Q_1 = h(T_{os} - T_{en}) \quad (4)$$

$$Q_2 = R\sigma(T_{os}^4 - T_{en}^4) \quad (5)$$

where h is the convective heat transfer coefficient, T_{os} is outer surface temperature of the stepped pipe specimen, T_{en} is the environment temperature, R is the radiation coefficient, σ is the Stefan-Boltzmann constant.

During the thermal fatigue process, the stepped pipe specimens were heated by high temperature water and cooled down rapidly after the shock of cold water. The thermal strain generated in the process was transformed into elastic strain and plastic strain by the joint action of geometric conditions and boundary constraints, and then the stress field was solved according to the constitutive relation of elastic-plastic mechanics.

$$\varepsilon_0 = \varepsilon_1 + \varepsilon_2 \quad (6)$$

$$\varepsilon_0 = \alpha \cdot \frac{\partial T}{\partial t} \quad (7)$$

$$[\sigma] = [D] \cdot [\varepsilon_1 + \varepsilon_2] \quad (8)$$

where ε_0 is the thermal strain, ε_1 is the elastic strain, ε_2 is the plastic strain, α is the coefficient of thermal expansion, $[\sigma]$ is the stress state, and $[D]$ is the elastic plastic stiffness matrix.

Then, the FEA file was imported into the crack growth analysis software FRANC3D, and the initial prefabricated crack parameters

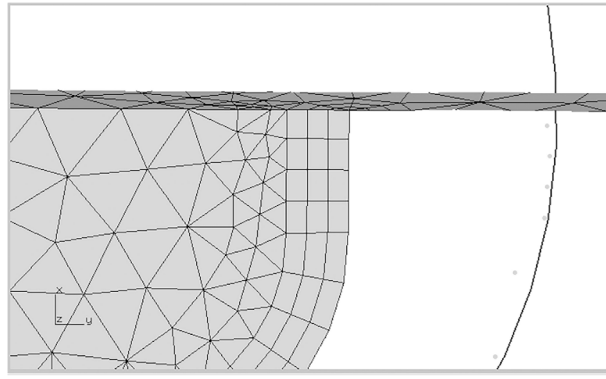


Fig. 9. Circumferential crack propagation front curve.

were defined for the model. FRANC3D would automatically complete mesh redivision and then submit the analysis to calculate the stress intensity factor. The meshing model of the stepped pipe specimen with initial prefabricated cracks is shown in Fig. 7. Next, the fatigue crack propagation of the stepped pipe was calculated using the Paris formula as the crack growth rate model [28,29].

$$da/dN = C(\Delta K)^m \quad (9)$$

where da/dN is the crack growth rate, a is the crack length, N is the number of fatigue cycles, ΔK is the amplitude of the stress intensity factor, and C, m are constants.

The maximum circumferential stress criterion was used as the fracture criterion to determine the direction of crack propagation. It was assumed that: (1) the crack propagated along the direction of the maximum circumferential stress; (2) when the circumferential stress in this direction was greater than the critical value, the crack began to propagate [30,31]. According to the theory of fracture mechanics, the circumferential stress field at the crack tip was

$$\sigma_{\theta\theta} = \frac{K_I}{\sqrt{2\pi r}} \left(\frac{3}{4} \cos \frac{\theta}{2} + \frac{1}{4} \cos \frac{3\theta}{2} \right) + \frac{K_{II}}{\sqrt{2\pi r}} \left(\frac{3}{4} \sin \frac{\theta}{2} + \frac{3}{4} \sin \frac{3\theta}{2} \right) \quad (10)$$

$$\sigma_{r\theta} = \frac{K_I}{\sqrt{2\pi r}} \left(\frac{1}{4} \sin \frac{\theta}{2} + \frac{1}{4} \sin \frac{3\theta}{2} \right) + \frac{K_{II}}{\sqrt{2\pi r}} \left(\frac{1}{4} \cos \frac{\theta}{2} + \frac{1}{4} \cos \frac{3\theta}{2} \right) \quad (11)$$

The conditions for determining the direction of crack propagation were

$$\frac{\partial \sigma_{\theta\theta}}{\partial \theta} \Big|_r = 0 \quad (12)$$

$$\frac{\partial^2 \sigma_{\theta\theta}}{\partial \theta^2} \Big|_r < 0 \quad (13)$$

moreover, $\sigma_{r\theta}=0$ was satisfied. According to Equations (10)-(13), the calculation expression of the crack propagation cracking angle could be obtained as follows

$$\theta = \arccos \theta \frac{3K_{II}^2 + K_I \sqrt{K_I^2 + 8K_{II}^2}}{K_I^2 + 9K_{II}^2} \quad (14)$$

In this analysis, the stepped pipe specimens were subjected to normal stress generated by tensile load, and the displacement of the upper and lower surfaces of the crack caused the crack to open, belonging to type I crack. The value of type II stress intensity factor K_{II} was very small and could be ignored. Therefore, only the value of type I stress intensity factor K_I needed to be considered, abbreviated as K .

In FRANC3D, the three-dimensional crack front was a spatial curve composed of a series of extrapolated nodes. Fig. 9 show the circumferential crack propagation front curve. For each node, the corresponding crack increment Δa_{nodei} was an artificially set ratio of the crack increment Δa_{user} . This ratio was related to the stress intensity factor at the crack front. The specific relationship formula for Δa_{nodei} and Δa_{user} was:

$$\Delta a_{nodei} = \Delta a_{user} \left(\frac{\Delta K_{nodei}}{\Delta K_{eq,mean}} \right)^n \quad (15)$$

where, Δa_{nodei} was the crack increment of crack front node i , Δa_{user} was the crack increment from the previous crack front to the next crack front defined by the user, ΔK_{nodei} was the stress intensity factor amplitude of crack front node i . $\Delta K_{eq,mean}$ was the average value

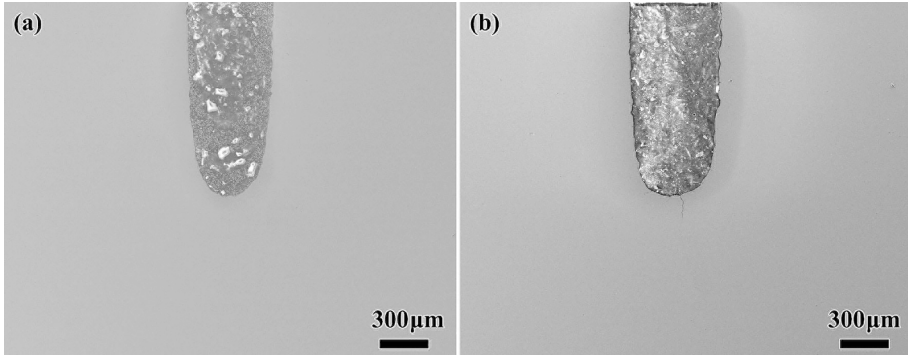


Fig. 10. Overall morphology of prefabricated defect: (a) specimen before thermal fatigue test, (b) Specimen 2 after thermal fatigue test.

of the stress intensity factor amplitude of the whole crack front, and exponential n was a user-defined parameter. Generally, the value of exponential n was the same as that of parameter m in the Paris formula.

According to the circumferential crack propagation increment set for cracks $\Delta a_{user} = 1$ mm, a total of nine propagation analysis steps were performed for crack propagation. After completing one of the current analysis steps, FRANC3D continued to call ABAQUS for dynamic crack finite element analysis to complete crack growth and mesh redvision. At the same time, the ΔK at the crack tip was calculated to obtain the crack tip ΔK curve of the crack growth step until the crack growth of nine analysis steps was completed. Finally, the stress field of fatigue crack propagation was obtained using ABAQUS software, and fatigue life can be obtained in FRANC3D.

4. Results and discussion

4.1. Thermal corrosion fatigue crack propagation

In order to analyze the crack propagation length and morphology of different specimens before and after thermal corrosion fatigue test, SEM is used to observe and measure the cross-section of the stepped pipe specimens. Fig. 10(a) shows the overall cross-sectional morphology of prefabricated defects before thermal fatigue test. It can be seen that the cross-sectional morphology of prefabricated defects is U-shaped, and there are no microcracks around the prefabricated defect. Fig. 10(b) shows the overall cross-sectional morphology of the prefabricated defects after thermal fatigue test of specimen 2, and it can be observed that there are many cracks propagating, and the cracks are all located at the U-shaped bottom.

Fig. 11 shows the crack propagation morphology of different 304 stainless steel weld joints stepped pipe specimens. There are seven cracks of different lengths at the prefabricated U-shaped bottom of specimen 2 (statistical crack length is greater than 10 μm), and the maximum crack length is 170 μm (Fig. 11(a)). It can be calculated that the average crack growth rate is 1.387×10^{-4} mm/cycle. Fig. 11b is an enlarged view of crack 2 in Fig. 11a, where multiple secondary cracks can be observed during the crack propagation, with obvious oxides at the crack tip. The process of crack propagation is mainly due to metal dissolution rather than pure mechanical fatigue, which is consistent with the slip dissolution model [22,32]. Fig. 11c shows the crack propagation morphology at the prefabricated U-shaped bottom of specimen 4. Five cracks of different lengths can be observed at the bottom, and the maximum crack length is 124 μm . It can be calculated that the average crack growth rate is 1.011×10^{-4} mm/cycle. Fig. 11d is an enlarged view of crack 1 in Fig. 11c, where the crack exhibits obvious deflection and bifurcation during propagation, and obvious oxides can also be observed. Fig. 11e shows the crack propagation morphology at the prefabricated U-shaped bottom of specimen 6. Two cracks of different lengths can be observed at the bottom, and the maximum crack length is 20 μm . It can be calculated that the average crack growth rate is 1.631×10^{-5} mm/cycle. Fig. 11f is an enlarged view of crack 2 in Fig. 11e, with a length of 18 μm . It can be considered as an early crack propagation process, where the crack tip is filled with oxides. Fig. 11(g-h) show the crack propagation morphology and local magnification at the prefabricated U-shaped bottom of specimen 8. No cracks can be observed, and it is considered that no crack growth occurs. Fig. 12 shows the relationship between thermal corrosion fatigue crack growth rate and cooling rate. It can be found that with the stepped pipe specimen away from the high pressure cold and hot water inlet, that is, with the gradual decrease of the cooling rate, the crack growth rate also gradually decreases. The thermal corrosion fatigue crack growth rate is exponentially related to the cooling rate, and the critical cooling rate of thermal fatigue crack propagation in the weld is 52 $^{\circ}\text{C}/\text{min}$. This is due to the fact that when cold water rapidly impacts the hot water inside the stepped pipe from the inlet, the temperature gradient near the inlet is larger, resulting in greater thermal stress on the stepped pipe specimen near the inlet. As it moves away from the inlet, the temperature gradient gradually decreases, and the thermal stress on the stepped pipe specimen also gradually decreases. Therefore, the thermal fatigue crack growth rate decreases with the decrease of thermal cyclic stress [33,34].

Fig. 13 shows the crack propagation morphology of 304 stainless steel base material stepped pipe specimens at different positions. There are three cracks of different lengths at the prefabricated U-shaped bottom of specimen 3, and the maximum crack length is 54 μm (Fig. 13(a)). It can be calculated that the average crack growth rate is 4.405×10^{-5} mm/cycle. Fig. 13b is an enlarged view of crack 2 in Fig. 13a, where multiple secondary cracks can also be observed during the crack propagation, with obvious oxides at the crack tip.

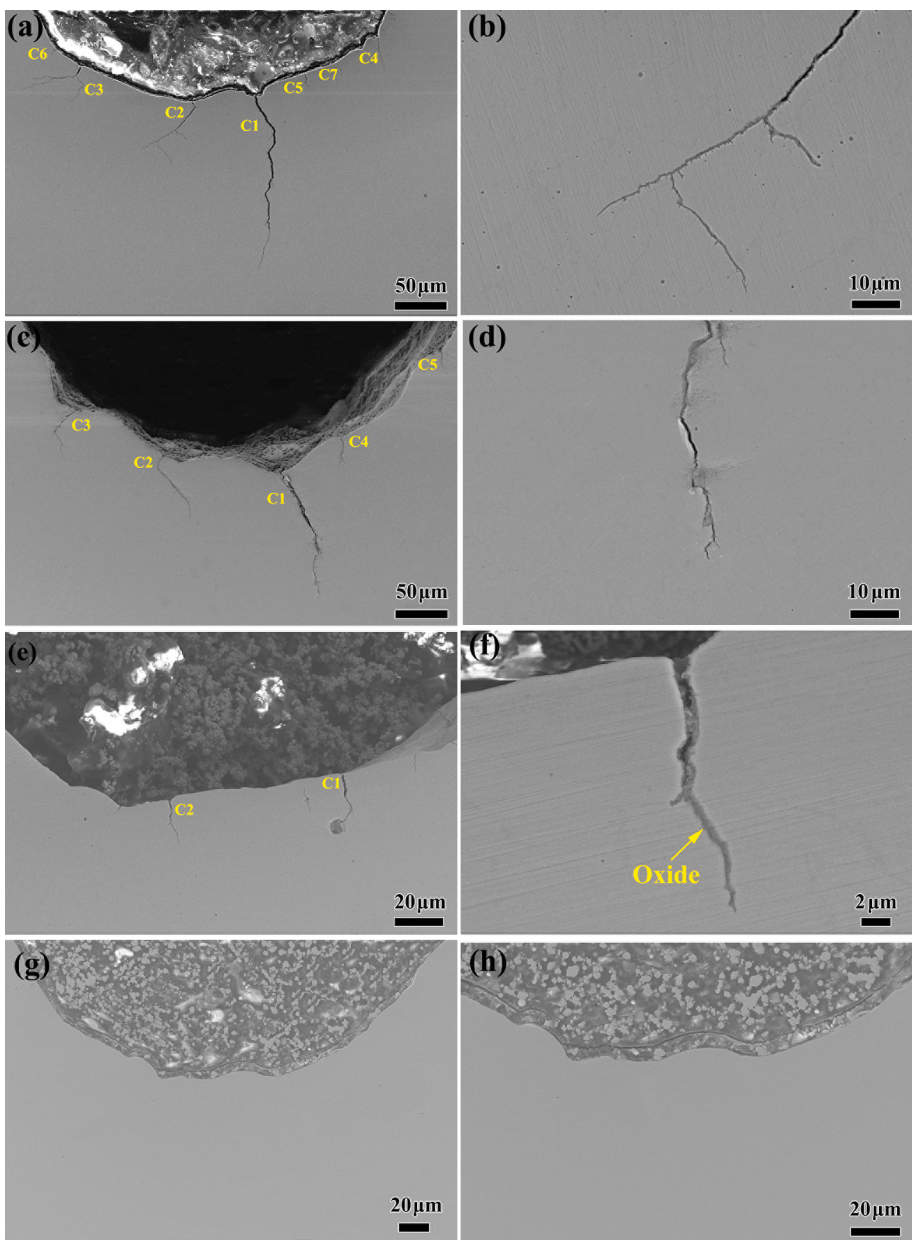


Fig. 11. Crack propagation morphology of different 304 stainless steel weld joints stepped pipe specimens: (a) stepped pipe specimen 2, (b) detailed crack propagation morphology of C2 in (a), (c) stepped pipe specimen 4, (d) detailed crack propagation morphology of C1 in (c), (e) stepped pipe specimen 6, (f) detailed crack propagation morphology of C2 in (e), (g) stepped pipe specimen 8, (h) enlarged view of (g).

Fig. 13c shows the crack propagation morphology at the prefabricated U-shaped bottom of specimen 5. Five cracks of different lengths can be observed at the bottom, and the maximum crack length is 12 μm . It can be calculated that the average crack growth rate is $9.788 \times 10^{-6} \text{ mm/cycle}$. **Fig. 13d** shows the crack propagation morphology at the prefabricated U-shaped bottom of specimen 7. No cracks can be observed, and it is considered that no crack growth occurs. Therefore, compared with the circumferential crack of the weld, the axial crack growth rate of the base material is slower. In addition, with the stepped pipe specimen away from the high pressure cold and hot water inlet, the crack growth rate of the base material also gradually decreases, and the thermal corrosion fatigue crack growth rate is also exponentially related to the cooling rate (**Fig. 12**). The critical cooling rates of thermal fatigue crack propagation in the base material is $112^\circ\text{C}/\text{min}$. The cooling rates of different specimens, as well as the specific number, length, and growth rate of cracks, are shown in **Table 3**. Since there is no crack propagation in specimens 9–12, their information is not counted in the table.

Fig. 14 shows the IPF maps and KAM maps from the EBSD analysis of fatigue crack propagation in different specimens. IPF map is usually used to show the crystal orientation of grains, and the orientation distribution is indicated by color, where red, green and blue

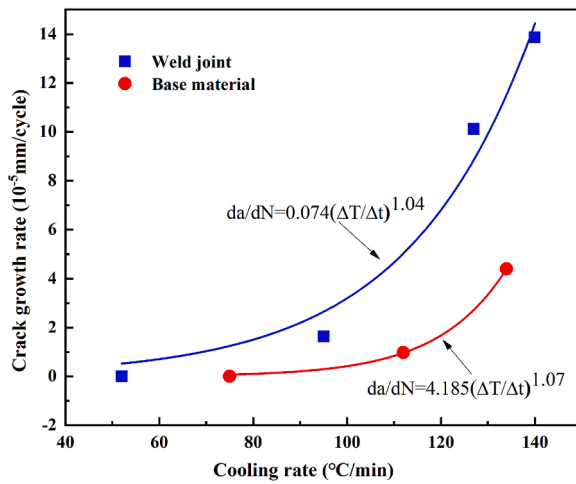


Fig. 12. Relationship between thermal corrosion fatigue crack growth rate and cooling rate.

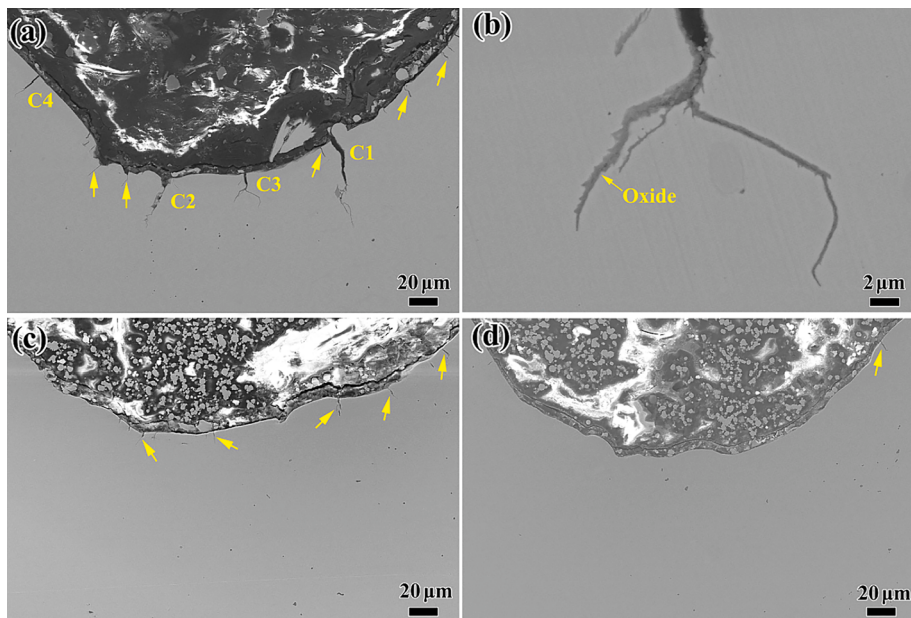


Fig. 13. Crack propagation morphology of different 304 stainless steel base material stepped pipe specimens: (a) stepped pipe specimen 3, (b) detailed crack propagation morphology of C3 in (a), (c) stepped pipe specimen 5, (d) stepped pipe specimen 7.

Table 3
Crack growth length and rate of different specimens.

Specimen number	Specimen type	Number of cracks (> 10 μm)	Maximum crack length	Cooling rate (°C/min, 90 s)	Crack growth rate (da/dN)
2	Weld joint	7	170 μm	140	1.387×10^{-4} mm/cycle
4	Weld joint	5	124 μm	127	1.011×10^{-4} mm/cycle
6	Weld joint	2	20 μm	95	1.631×10^{-5} mm /cycle
8	Weld joint	0	0	52	0
3	Base material	3	54 μm	134	4.405×10^{-5} mm /cycle
5	Base material	1	12 μm	112	9.788×10^{-6} mm /cycle
7	Base material	0	0	75	0

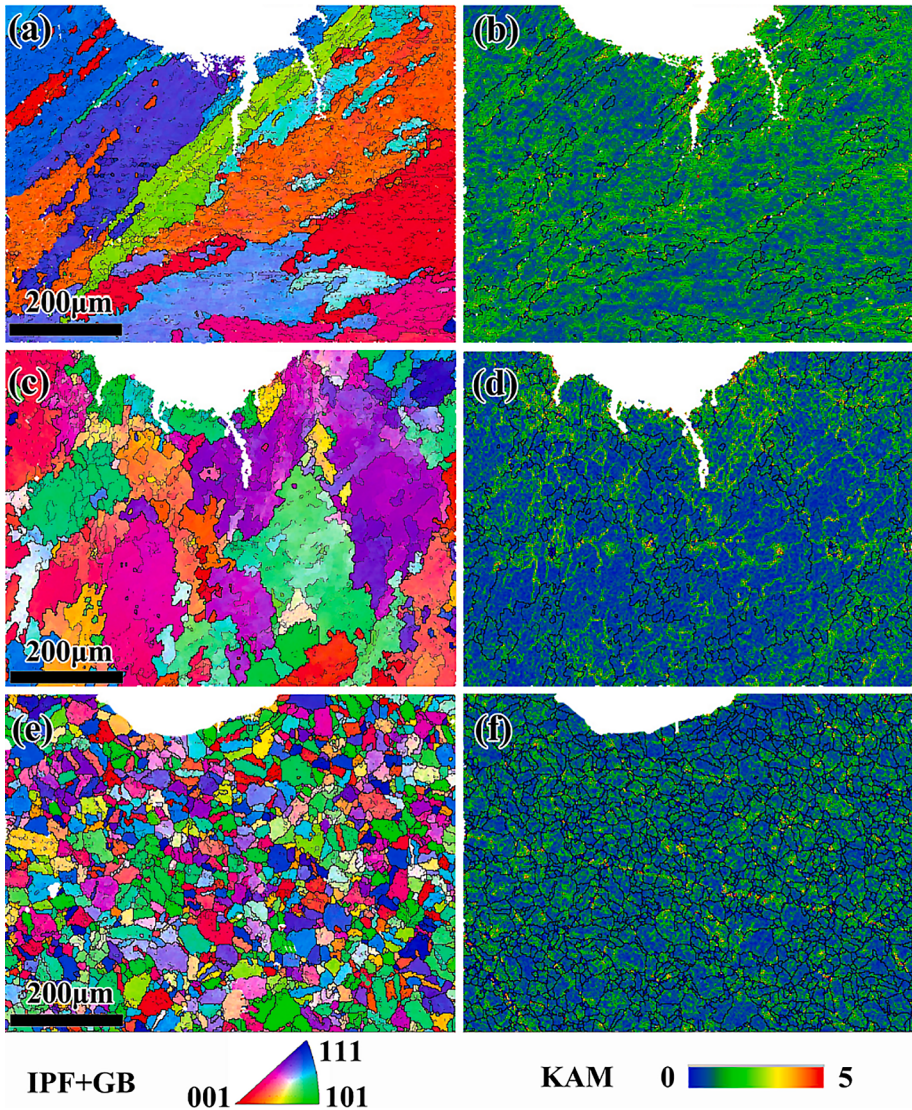


Fig. 14. EBSD analysis of fatigue crack propagation in different specimens: IPF maps of (a) weld joint stepped pipe specimen 2, (c) weld joint stepped pipe specimen 4, and (e) base material stepped pipe specimen 5; KAM maps of (b) weld joint stepped pipe specimen 3, (d) weld joint stepped pipe specimen 5, and (f) base material stepped pipe specimen 5.

represent $\langle 100 \rangle$, $\langle 101 \rangle$ and $\langle 111 \rangle$ orientations. Fig. 14a shows the IPF map of the weld joint stepped pipe specimen 2, with a gradation in color appearing in most grains, indicating the development of substructures during fatigue crack propagation. The grain size of the weld is about 100 μm , and the cracks all show transgranular cracking during the propagation. Fig. 14b shows the KAM map of the weld joint stepped pipe specimen 2, where blue represents the minimum KAM value and red represents the maximum KAM value. KAM or LocMis can qualitatively reflect the homogenization degree of plastic deformation, and the higher value indicates the higher plastic deformation degree or the higher defect density [35,36]. It can be observed that the entire prefabricated defect area undergoes significant deformation, with higher degrees of deformation on both sides of crack propagation. Fig. 14c shows the IPF map of the weld joint stepped pipe specimen 4, and some grains at the bottom of the prefabricated defect also undergo color gradient. The crack propagation length of stepped pipe specimen 4 is smaller than that of specimen 2, and all cracks exhibit transgranular cracking. Fig. 14d shows the KAM map of the weld joint stepped pipe specimen 4. Compared to specimen 2, the specimen 4 has a lower strain level and only exhibits higher strain near the grain and crack propagation at the bottom of the prefabricated defect. Fig. 14e shows the IPF map of the base material stepped pipe specimen 5, the grains basically maintain the near single crystal orientation of the uniform IPF color shade. The grain size of the base material is about 28 μm , and the cracks also show transgranular cracking during the propagation. Fig. 14f shows the KAM map of the base material stepped pipe specimen 5, with low deformation in the bottom area of the prefabricated defects. Compared with the base metal specimen, the residual strain of the weld specimen is larger, which promotes crack propagation [15].

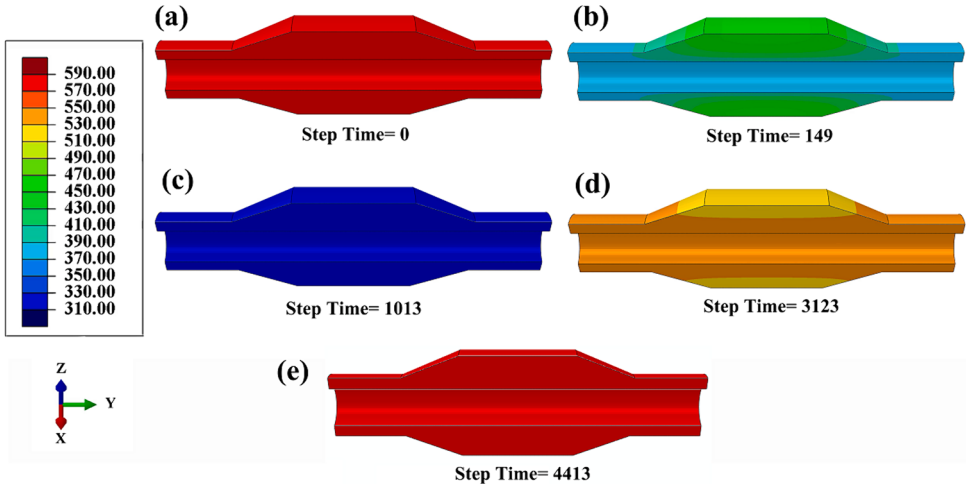


Fig. 15. Temperature field distribution at different stages of a cycle (actual measured temperature of the stepped pipe specimens in the process of cold and hot water circulation was measured by thermocouple, Fig. 7(c): (a) step time = 0, (b) step time = 149, (c) step time = 1013, (d) step time = 3123, (e) step time = 4413).

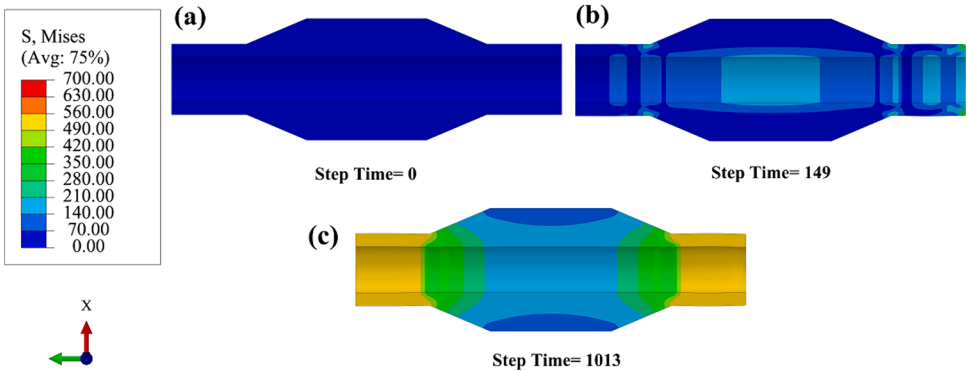


Fig. 16. Stress field distribution at different stages of a cycle: (a) step time = 0, (b) step time = 149, (b) step time = 1013.

4.2. Numerical evaluation of fatigue crack propagation

The temperature of the stepped pipe specimens in the process of cold and hot water circulation was measured by thermocouple. Fig. 15 shows the temperature field distribution results at different stages of a cycle obtained by inputting the measured temperature into the simulation software. At the beginning, the stepped pipe specimen was heated to 325 °C (Fig. 15a), and then under the shock of cold water, the temperature of the stepped pipe specimen rapidly decreased, and after only 149 s, the temperature dropped to 100 °C (Fig. 15b). Subsequently, the temperature slowly decreased to 38 °C (Fig. 15c), followed by a gradual increase in temperature to 325 °C (Fig. 15(d–e)), with each cycle lasting 3660 s. Fig. 16 shows the stress field distribution results at different stages of a cycle calculated by temperature-displacement coupling solver. It could be seen that with the shock of cold water, the stepped pipe specimen gradually experienced greater stress. In the alternating process of hot and cold water, the stepped pipe specimen was subjected to cyclic stress, which will promote the crack propagation. The cyclic stress used in numerical simulation of fatigue crack growth came from thermal cyclic stress. Fig. 17 shows the numerical simulation results of the circumferential crack propagation under the action of stress field after prefabricated cracks. According to equation (15), since in each subsequent analysis step, the propagation size of each node at the crack front was the ratio of the artificially set crack increment, which varied with the ΔK at each crack front, the propagation size of each node at the crack front in a certain increment step was different. From step one to nine, there were nine analysis steps, each step of the crack front presented a curved shape, and the curve shape was different. The schematic diagram of circumferential crack propagation path for the stepped pipe specimen in nine steps is shown in Fig. 17(a). Fig. 17(b) shows the crack tip ΔK curve of the nine crack growth steps. Under the action of cyclic stress, the crack growth rate gradually increased and the crack tip ΔK also gradually increased. Fig. 17(c–e) show the stress field distribution of the first, third, and ninth steps of circumferential crack propagation, respectively. It can be found that stress concentration was continuously generated at the crack tip, and the crack continued to propagate outward along the circumferential direction. In addition, after 77 s of cold water shock, the stress field at the crack tip was maximum.

After completing nine analysis steps of crack propagation, the relationship between crack propagation length and number of cycles

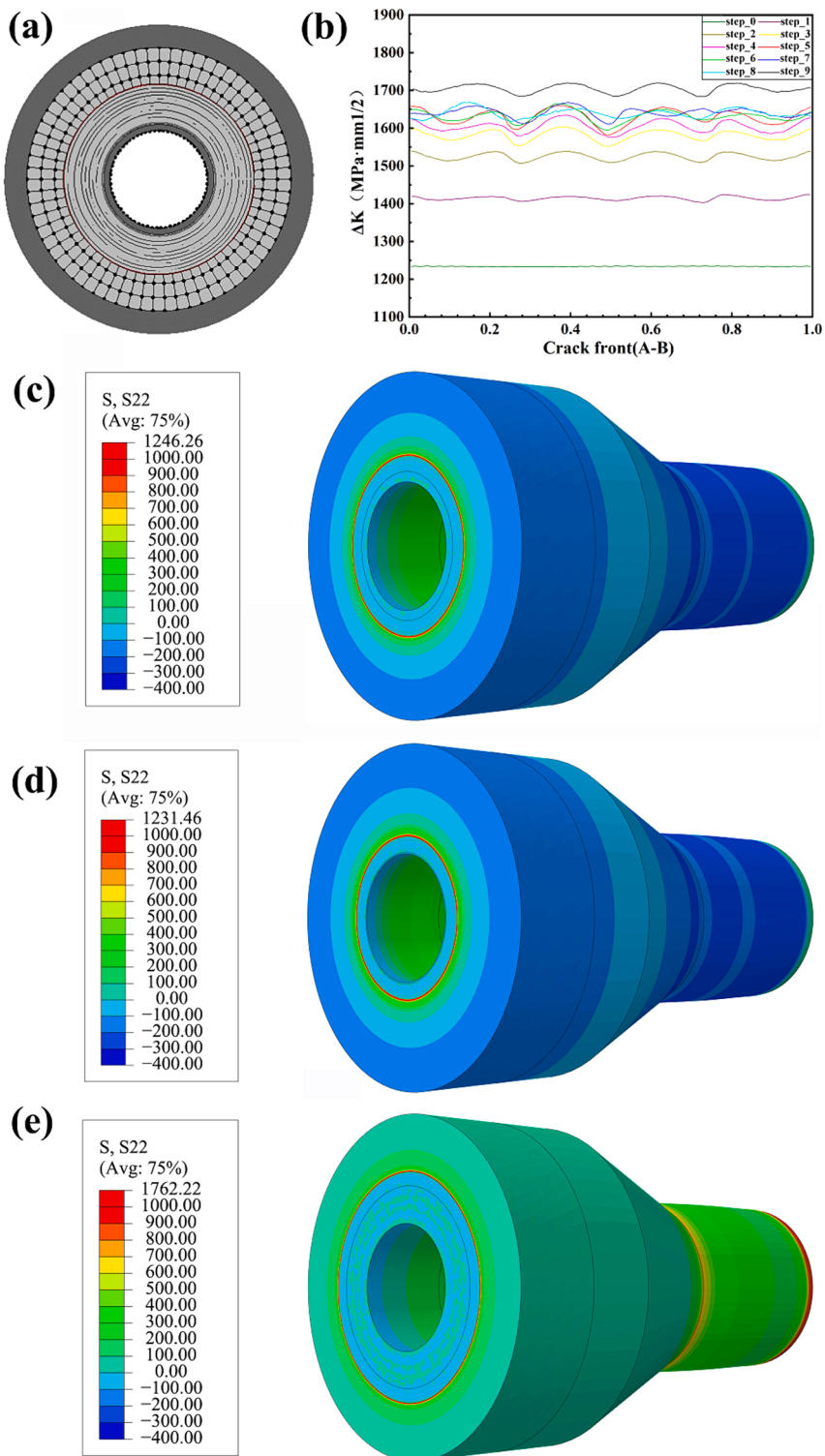


Fig. 17. Numerical simulation results of circumferential crack propagation: (a) schematic diagram of fatigue crack propagation path in nine steps, (b) crack tip ΔK curve of the nine crack growth steps, stress field distribution of the (c) first (d) third and (e) ninth step of crack growth.

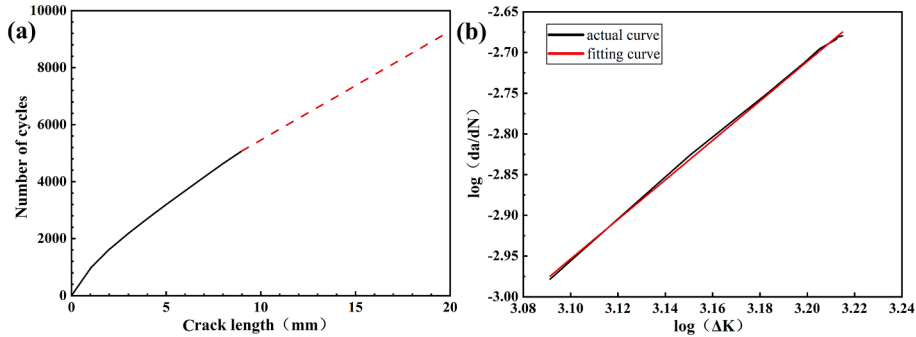


Fig. 18. Results of circumferential crack growth analysis: (a) relationship between crack growth length and number of cycles, (b) double logarithmic relationship curve between crack growth rate $\log(da/dN)$ and $\log(\Delta K)$.

was obtained, and an a - N curve was plotted, as shown in Fig. 18(a). Then, the crack growth rate $\log(da/dN)$ and $\log(\Delta K)$ double logarithmic relationship curve was obtained by fitting, as shown in Fig. 18(b) and its relationship expression was

$$\log(da/dN) = 2.43\log(\Delta K) - 10.47 \quad (16)$$

According to the crack growth rate model (9), it can be obtained

$$da/dN = 2.2 \times 10^{-11} (\Delta K)^{2.43} \quad (17)$$

Through simulation calculation, it was found that after 1226 cycles of cold and hot stress, the circumferential crack propagated by 1.41 mm. Compared with the thermal fatigue experimental results propagated by 170 μm , the simulated results were 8.3 times larger than the experimental results. This was mainly caused by two reasons, the first was that when the prefabricated circumferential defect was simulating fatigue crack propagation, the crack propagated outward along the whole circumferential direction, and the crack propagation resistance was relatively small. However, in actual thermal fatigue experiment, cracks only propagated in the local area of the prefabricated defect, and the crack propagation was limited by the nearby interface, which required overcoming the surface energy from the circumferential direction, resulting in a higher resistance to crack propagation. The second was that when simulating fatigue crack propagation, the boundary condition of the stepped pipe specimen was fixed on one side and free on the other side, and the crack propagation was fast under the tensile stress orthogonal to the crack surface. However, in actual thermal fatigue experiment, all the stepped pipe specimens were connected by welding, with both ends fixed on the bench. When subjected to hot and cold cyclic tensile stress, the crack opening was limited due to the constraints of both sides of the bench, which hindered the crack propagation forward. Therefore, the thermal fatigue crack growth rate obtained by numerical simulation was much higher than that in the actual thermal fatigue experiment. However, the crack growth rate model could be modified by increasing the correction factor f_1 , as shown in equation (18).

$$da/dN = f_1 C(\Delta K)^m \quad (18)$$

5. Conclusions

In this paper, the thermal corrosion fatigue crack propagation behavior of 304 stainless steel stepped pipe base material and weld structure under transient water temperature changes was studied, and the thermal fatigue crack propagation life was predicted based on numerical simulation method. The major results could be drawn as follows:

- 1) A dual loop circulating water thermal fatigue test method based on high-throughput testing technology had been established, and the influence of transient temperature changes on the thermal fatigue performance of pipeline structures was successfully simulated.
- 2) The cooling rate had a significant effect on the thermal fatigue crack growth rate in stepped pipes. As the stepped pipe specimen moved away from the inlet of hot and cold water, the fatigue crack growth rate gradually decreased with the decrease of cooling rate, and the fatigue crack growth rate was exponentially related to the cooling rate.
- 3) Both the base material and weld of the stepped pipe showed a transgranular cracking mode, and propagated continuously by slip-oxidation mechanism. Compared with the fine equiaxed grain of the base material, the grain in the weld was coarse and the residual strain was large, and the crack growth rate of the weld was obviously higher. The critical cooling rates of thermal fatigue crack propagation in the weld and base material were 52 $^{\circ}\text{C}/\text{min}$ and 112 $^{\circ}\text{C}/\text{min}$, respectively.
- 4) By combining finite element thermo-mechanical coupling simulation and three-dimensional crack propagation analysis software, the thermal fatigue crack propagation life of stepped pipes was successfully predicted. A Paris model was established between the thermal fatigue crack propagation rate and stress intensity factor of stepped pipes, and the model was modified based on the results of thermal corrosion fatigue experiments.

CRediT authorship contribution statement

Z.H. Li: Investigation, Formal analysis, Writing – original draft. **Y.M. Han:** Methodology, Investigation, Data curation. **Y.G. Zhao:** Visualization, Software. **S.L. Yang:** Methodology, Conceptualization. **Z.M. Zhong:** Validation, Resources. **Y.H. Lu:** Supervision, Writing – review & editing, Funding acquisition.

Declaration of competing interest

The authors declare that they have no known competing financial interests or personal relationships that could have appeared to influence the work reported in this paper.

Data availability

The authors are unable or have chosen not to specify which data has been used.

Acknowledgements

The authors acknowledge the financial supports from the Opening Project Fund of Materials Service Safety Assessment Facilities (MSAF-2021-104).

References

- [1] M. Dougdag, R. Fernandez, D. Lamberts, Risk reassessment of thermal striping due to a macro-crack pre-existent in nuclear reactors at high temperature, *Ann. Nucl. Energy* 174 (2022) 109152.
- [2] Z.C. Guo, J.Q. Zou, Y.Q. Chen, K.L. Xu, T. Lu, B. Liu, Monitoring of wall temperature fluctuations for thermal fatigue in a horizontal mixing T-junction pipe, *Prog. Nucl. Energ.* 104 (2018) 298–305.
- [3] M. Hayashi, K. Enomoto, T. Saito, T. Miyagawa, Development of thermal fatigue testing apparatus with BWR water environment and thermal fatigue strength of austenitic stainless steels, *Nucl. Eng. Des.* 184 (1998) 113–122.
- [4] O.C. Garrido, S.E. Shawish, L. Cizelj, Uncertainties in the thermal fatigue assessment of pipes under turbulent fluid mixing using an improved spectral loading approach, *Inter. J. Fatigue* 82 (2016) 550–560.
- [5] N. Haddar, A. Fissolo, V. Maillot, Thermal fatigue crack networks: an computational study, *Inter. J. Solids Struct.* 42 (2005) 771–788.
- [6] N. Haddar, A. Fissolo, 2D simulation of the initiation and propagation of crack array under thermal fatigue, *Nucl. Eng. Des.* 235 (2005) 945–964.
- [7] J.M. Wang, Y.L. Wu, T.Y. Zhu, K. Chen, J.N. Mei, F. Xue, H.T. Sun, W.J. Ma, Y.H. Wang, P.L. Andresen, L.F. Zhang, Effect of thermal aging on the environmental assisted cracking behavior of 308L weld metal in high temperature water, *Corros. Sci.* 211 (2023) 110902.
- [8] J. Xiao, T. Xiao, Y.Q. Zheng, H. Wang, Y. Chen, S.Y. Qiu, X. Gong, Corrosion fatigue crack growth behavior of 316NG heat affected zone in simulated pressurized water reactor environment, *J. Nucl. Mater.* 537 (2020) 152259.
- [9] Z.H. Li, Y.H. Lu, X.Y. Wang, Modeling of stress corrosion cracking growth rates for key structural materials of nuclear power plant, *J. Mater. Sci.* 55 (2020) 439–463.
- [10] R. Tunstall, D. Laurence, R. Prosser, A. Skillen, Large eddy simulation of a T-junction with upstream elbow: the role of dean vortices in thermal fatigue, *Appl. Therm. Eng.* 107 (2016) 672–680.
- [11] Z.Y. Su, K. Inaba, A. Karmakar, D. Apurba, Fluid structure interaction simulation of thermal striping in a t-junction pipe made of functionally graded material, *Int. J. Mech. Mater. Des.* 18 (2022) 461–473.
- [12] M. Merola, Normative issues in thermal fatigue design of nuclear components, *Nucl. Eng. Des.* 158 (1995) 351–361.
- [13] K. Thamaraiselvi, S. Vishnuvardhan, Fracture studies on reactor pressure vessel subjected to pressurised thermal shock: a review, *Nucl. Eng. Des.* 360 (2020) 110471.
- [14] J.B. Tan, X.Q. Wu, E.H. Han, W. Ke, X. Wang, H.T. Sun, Strain-rate dependent fatigue behavior of 316LN stainless steel in high-temperature water, *J. Nucl. Mater.* 489 (2017) 33–41.
- [15] Y.J. Ma, Z.Y. Zhang, X. Zhang, H.F. Yin, B.B. Liang, J.B. Tan, X.Q. Wu, E.H. Han, W. Ke, Effects of strain rate on low-cycle fatigue crack growth behavior of 316LN weld metal in high-temperature pressurized water, *Corros. Sci.* 199 (2022) 110169.
- [16] Z.Y. Zhang, J.B. Tan, X.Q. Wu, E.H. Han, W. Ke, Synergistic effect of mechanical and environmental damages of 316LN stainless steel under different fatigue strain amplitudes in high-temperature pressurized water, *Mater. Sci. Eng. A* 743 (2019) 243–250.
- [17] Z.Y. Zhang, J.B. Tan, X.Q. Wu, E.H. Han, W. Ke, J.C. Rao, Effects of temperature on corrosion fatigue behavior of 316LN stainless steel in high-temperature pressurized water, *Corros. Sci.* 146 (2019) 80–89.
- [18] H.C. Wu, C.T. Li, K.W. Fang, F. Xue, B. Yang, X.P. Song, Effect of grain size on the low cycle fatigue behavior of 316LN stainless steel in high temperature water, *Mater. Corros.* 68 (2017) 1180–1189.
- [19] Y.J. Ma, Z.Y. Zhang, J.B. Tan, X.Q. Wu, X. Wang, E.H. Han, W. Ke, Effect of surface roughness on low-cycle fatigue behaviors of 316LN stainless steel in borated and lithiated high-temperature pressurized water, *Corros. Sci.* 209 (2022) 110792.
- [20] Z.H. Li, Y.H. Lu, C. Hong, Y.G. Zhao, Y.M. Han, T. Shoji, Corrosion fatigue damage mechanism and life evaluation of inconel alloy 690TT steam generator tube in high temperature pressurized water, *Corros. Sci.* 212 (2023) 110953.
- [21] J.B. Tan, X.Q. Wu, E.H. Han, W. Ke, X.Q. Liu, F.J. Meng, X.L. Xu, Corrosion fatigue behavior of alloy 690 steam generator tube in borated and lithiated high temperature water, *Corros. Sci.* 89 (2014) 203–213.
- [22] Z.H. Li, Y.H. Lu, L. You, X.F. Zhang, L. Wang, D.H. Tian, W.D. Zhang, T. Shoji, Effect of temperature on corrosion fatigue behavior of inconel alloy 690TT steam generator tube, *Corros. Sci.* 227 (2024) 111741.
- [23] Z.H. Li, C. Hong, Y.G. Zhao, Y. Hu, Y.H. Lu, T. Shoji, Cyclic deformation behavior and cracking mechanism of inconel alloy 690TT steam generator tube at elevated temperature, *Mater. Character.* 190 (2022) 111935.
- [24] Y.D. Xiong, Y. Watanabe, Y. Shibayama, N. Mary, X.Y. Zhong, Low-cycle fatigue behaviors of 316LN austenitic stainless steel in borated and lithiated high temperature water with different levels of dissolved oxygen, *Corros. Sci.* 176 (2020) 109048.
- [25] Y.D. Xiong, Y. Watanabe, Y. Shibayama, Effects of dissolved hydrogen on low-cycle fatigue behaviors and hydrogen uptake of 316LN austenitic stainless steel in simulated pressurized water reactor primary water, *Inter. J. Fatigue* 134 (2020) 105457.
- [26] J.B. Tan, X.Q. Wu, E.H. Han, W. Ke, X.Q. Liu, F.J. Meng, X.L. Xu, Role of TiN inclusion on corrosion fatigue behavior of alloy 690 steam generator tubes in borated and lithiated high temperature water, *Corros. Sci.* 88 (2014) 349–359.
- [27] K.C. Mills, Recommended values of thermophysical properties for selected commercial alloys, Woodhead Publishing, 2002.
- [28] P.C. Paris, F. Erdogan, A critical analysis of crack propagations laws, *J. Basic Eng. Trans. Am. Soc. Mech. Eng.* 85 (1963) 528–534.

- [29] D. Rozumek, S. Faszynka, Surface cracks growth in aluminum alloy AW-2017A-T4 under combined loadings, *Eng. Fract. Mech.* 226 (2020) 106896.
- [30] F. Erdogan, G.C. Sih, On the crack extension in plates under plane loading and transverse shear, *ASME, J. Basic Eng.* 85 (1963) 519–525.
- [31] H.L. Wang, S. Tanaka, S. Oterkus, E. Oterkus, Study on two-dimensional mixed-mode fatigue crack growth employing ordinary state-based peridynamics, *Theor. Appl. Fract. Mech.* 124 (2023) 103761.
- [32] J.M. Wang, H.Z. Su, K. Chen, D.H. Du, L.F. Zhang, Y.D. Sun, Corrosion fatigue crack growth behavior of alloy 52 M in high-temperature water, *J. Nucl. Mater.* 528 (2020) 151848.
- [33] H.P. Seifert, S. Ritter, H.J. Leber, Corrosion fatigue crack growth behaviour of austenitic stainless steels under light water reactor conditions, *Corros. Sci.* 55 (2012) 61–75.
- [34] K. Chen, J.M. Wang, D.H. Du, P.L. Andresen, L.F. Zhang, dK/da effects on the SCC growth rates of nickel base alloys in high-temperature water, *J. Nuclear Mater.* 503 (2018) 13–21.
- [35] Z.H. Li, Y.H. Lu, C. Hong, Y.G. Zhao, W.D. Zhang, T. Shoji, Effects of foreign object damage on high-cycle fatigue behavior of inconel alloy 690TT steam generator tubes, *Eng. Fract. Mech.* 292 (2023) 109660.
- [36] T. Nagoshi, S. Kozu, Y. Inoue, B.E. O'Rourke, Y. Harada, Fatigue damage assessment of SUS316L using EBSD and PALS measurements, *Mater. Character.* 154 (2019) 61–66.